Quantum phase transition from triangular to stripe charge order in NbSe2

(Article begins on next page)

Quantum phase transition from triangular to stripe charge order in NbSe₂

Anjan Soumyanarayanan[a,b,1], Michael M. Yee[a], Yang He[a], Jasper van Wezel[c,d,2], Dirk J. Rahn[e], Kai Rossnagel[e], E. W. Hudson[f], Michael R. Norman[c], and Jennifer E. Hoffman[a,1]

[a]Department of Physics, Harvard University, Cambridge, MA 02138; [b]Department of Physics, Massachusetts Institute of Technology, Cambridge, MA 02139; [c]Materials Science Division, Argonne National Laboratory, Argonne, IL 60439; [d]H. H. Wills Physics Laboratory, University of Bristol, Bristol BS8 1TL, United Kingdom; [e]Institute of Experimental and Applied Physics, University of Kiel, 24098 Kiel, Germany; and [f]Department of Physics, Pennsylvania State University, State College, PA 16802

The competition between proximate electronic phases produces a complex phenomenology in strongly correlated systems. In particular, fluctuations associated with periodic charge or spin modulations, known as density waves, may lead to exotic superconductivity in several correlated materials. However, density waves have been difficult to isolate in the presence of chemical disorder, and the suspected causal link between competing density wave orders and high-temperature superconductivity is not understood. Here we used scanning tunneling microscopy to image a previously unknown unidirectional (stripe) charge-density wave (CDW) smoothly interfacing with the familiar tridirectional (triangular) CDW on the surface of the stoichiometric superconductor NbSe₂. Our low-temperature measurements rule out thermal fluctuations and point to local strain as the tuning parameter for this quantum phase transition. We use this quantum interface to resolve two longstanding debates about the anomalous spectroscopic gap and the role of Fermi surface nesting in the CDW phase of NbSe₂. Our results highlight the importance of local strain in governing phase transitions and competing phenomena, and suggest a promising direction of inquiry for resolving similarly longstanding debates in cuprate superconductors and other strongly correlated materials.

competing order | scanning tunneling spectroscopy | transition metal dichalcogenides

Whereas a classical phase transition separates two states of matter at different temperatures, two ordered ground states of a material at zero temperature are separated by a quantum critical point (QCP). The competition between proximate ordered phases near the QCP can dramatically influence a large region of the phase diagram (1). Whereas the fluctuations from competing quantum states lead to exotic physics even at higher temperatures, low-temperature studies of these states may lead to a better understanding of the root of the competition. Density waves—charge- or spin-ordered states of collective origin driven by instabilities of the Fermi surface (FS)—exist in close proximity to superconductivity (SC) in several classes of correlated materials (2–4), and various proposals emerged recently to study their interplay in the presence of strong inhomogeneity in these systems (5). In this light, it is surprising that charge-density waves (CDWs) are not fully understood, even in the weakly correlated and stoichiometric transition metal dichalcogenides (TMDCs). Whereas a classic CDW arises from strong FS nesting, resulting in a sharply peaked susceptibility and a Kohn anomaly at the CDW wavevector, the quasi-2D TMDCs are known to deviate from this picture (6, 7).

NbSe₂ is a layered TMDC that has generated much recent interest (8–10) as a model system for understanding the interplay of the CDW and SC phases with onset at $T_{CDW} \sim 33$ K and $T_{SC} \sim 7$ K respectively (11, 12). Despite extensive study (9, 13–16), several key facts about its familiar tridirectional (3Q) CDW remain unresolved, including the role of FS nesting in determining its wavevector $\vec{q}_{3Q}$ and the magnitude of the spectral gap and its

role in the energetics of the transition. First, angle-resolved photoemission (ARPES) studies have been unable to uniquely identify $\vec{q}_{3Q}$-nested FS regions in NbSe₂ (9, 13, 16–20). Meanwhile, recent studies indicate a broadly peaked susceptibility and a soft phonon over a range of wavevectors around $\vec{q}_{3Q}$ (6, 15, 16), suggesting instead that the q-dependence of the electron–phonon coupling might play an important role in driving the transition. Second, kinks in tunneling spectra at ± 35 mV ($\pm \varepsilon_K$), historically identified as gap edges, correspond to an anomalously large energy scale for the corresponding T_{CDW} ($2\varepsilon_K/3.5 k_B T_{CDW} \sim 7.05$) (21), whereas recent ARPES studies indicate a much smaller gap, ~3–5 mV (13, 16).

Our discovery, by low-temperature scanning tunneling microscopy (STM), of a unidirectional (1Q) CDW with distinct wavelength and tunneling spectra from the 3Q CDW, in conjunction with band structure calculations, allows us to resolve both longstanding questions of the wavevector and the gap. First, the distinct wavelengths demonstrate that FS nesting plays a negligible role in setting their magnitude. Second, the distinct tunneling spectra of the 1Q CDW region help us disentangle the 3Q CDW spectra to expose a particle-hole asymmetric gap, riding on top of a strong inelastic background.

Results

Fig. 1A shows a topographic image of a locally commensurate ($3a_0$) CDW on 2H-NbSe₂. Its microscopic 3Q nature is confirmed by the existence of a secondary CDW peak in the Fourier transform (FT) in Fig. 1B, in contrast to bulk measurements (10). Phase slips result in an overall periodicity of $\lambda_{3Q} \simeq 3.05\, a_0$, corresponding to $\vec{q}_{3Q} \simeq 0.328\, \vec{Q}_0$, where $\vec{Q}_0$ is the Bragg vector (10, 11, 22). Our primary experimental discovery is shown in Fig. 2A, where regions of unidirectional (1Q) CDW with unique wavevector $\vec{q}_{1Q}$ along a single 3Q direction form an atomically smooth interface with the 3Q CDW. The absence of atomic lattice discontinuities rules out the possibility of an NbSe₂ polytype interface (23). Although other TMDCs are known to exhibit a thermally induced triclinic CDW state that varies with doping near T_{CDW} (22, 24), no such anisotropy has been reported in 2H-NbSe₂. Moreover, our observations are at temperatures $T \ll T_{CDW}$, where thermal fluctuations are

PHYSICS

Fig. 1. STM of the 3Q CDW. (*A*) Atomic resolution topograph showing the ~3 a_0 periodic CDW. Yellow lines are overlaid on a one-atom shift of the CDW maximum (phase slip). (*Inset*) Crystal structure of 2H-NbSe$_2$, with layers of Nb (green) atoms sandwiched between layers of Se (orange) atoms. (*B*) FT of a larger (~45 nm) topograph, displaying a 3Q CDW. Primary CDW wavevectors, $\vec{q}_1$ and $\vec{q}_2$ (yellow circles); a secondary CDW wavevector, $\vec{q}_1 + \vec{q}_2$ (blue circle); and Bragg vectors (dashed red circles) are indicated. (*C*) Average dI/dV spectrum acquired from the area in *A*, showing kinks at ~ ±35 mV (±ε_K), the minimum ε_{min} offset from $\varepsilon_F (V_{bias} = 0)$ by ~17 mV, and marked asymmetry about ε_F. Setpoint parameters: sample bias, $V_{sample} = -50$ mV (*A*), -60 mV (*B*) and -80 mV (*C*); junction resistance, $R_J = 2.5$ GΩ (*A*), 0.1 GΩ (*B*), and 0.4 GΩ (*C*); and root mean square (RMS) lock-in excitation, $V_{rms} = 3.5$ mV (*C*).

insignificant, implying that the 1Q CDW is a distinct quantum phase.

The 1Q CDW regions take the form of elevated topographic ribbons, exemplified in Fig. 2 *B* and *C*, suggesting a strain-induced phase (*SI Text II*). The observation of *Y*-junctions between ribbons with differently oriented $\vec{q}_{1Q}$ rules out extrinsic uniaxial strain and suggests instead locally varying strain, perhaps because of underlying defects causing nanoscale buckling of the top few atomic layers. From a survey of several ribbons, we place upper bounds of 3% on the vertical strain and 0.06% on the lateral strain (*SI Text II*).

Fig. 3 *A* and *B* show the dominant Fourier peak for the 1Q modulation, $\vec{q}_{1Q} \simeq (2/7)\vec{Q}_0$, corresponding to a wavelength, $\lambda_{1Q} \simeq 3.5\ a_0$. No similar periodicity or rich harmonic structure has been reported thus far in any TMDC system (12). We develop a phenomenological understanding of the 1Q harmonic structure following McMillan's Landau theory (22, 25). Rather than a uniform 3.5 a_0 charge modulation, the system could lower its energy by locking the charge modulation to the lattice with 3 a_0 periodicity. This would require compensation by a one-atom phase slip every two oscillations, corresponding to a $2\pi/3$ discommensuration, as shown in Fig. 3*C* (22). The resulting har-

monic structure shown in Fig. 3*D* reproduces all observed peak positions. Moreover, the rich harmonic content we observe is another indication of the strong coupling of the electronic modulation to the lattice. An even better agreement with relative peak heights might be obtained by considering spatial variations in the order parameter amplitude (22).

The stark contrast between our observation of two CDW wavevectors $\vec{q}_{1Q}$ and $\vec{q}_{3Q}$ of the same orientation but with 13% difference in magnitude, and the recent X-ray measurements reported by Feng et al. (10), provides strong evidence against FS nesting at one particular wavevector as a driving force for either CDW. Although our 13% wavevector difference arose from moderate anisotropic strain (up to 0.06% in-plane), Feng et al. applied hydrostatic pressure sufficient to induce in-plane lattice distortions up to 1.6%, yet observed no measurable deviation of the CDW wavevector from q_{3Q} (10). The observed insensitivity of q_{3Q} to hydrostatic pressure would clearly indicate that the FS does not qualitatively change in the presence of even relatively large lattice distortions, and thus would rule out a change in the FS as the source of our observed 13% wavevector difference. Furthermore, consistent with our experiment and with previous calculations (6, 15, 16), we find no sharp peak in the susceptibility
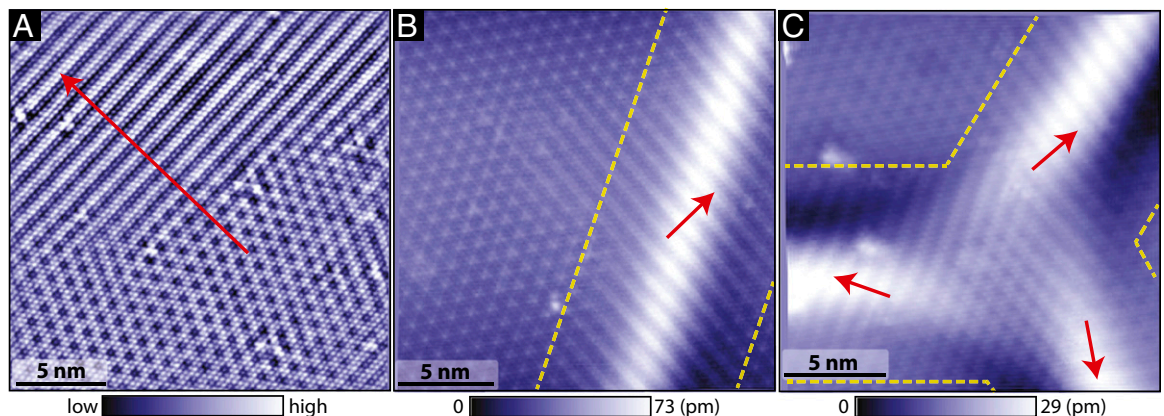
Fig. 2. The 1Q–3Q interface. (*A*) Topograph showing an atomically smooth interface between the 3Q (*Bottom*) and 1Q (*Top*) CDWs. (*B*) Topograph showing formation of 1Q CDW along a "ribbon." Ribbons are typically 10–20 nm in width and elevated by 20–40 pm. Dashed yellow lines indicate the approximate extent of the ribbon; the red arrow points along the 1Q CDW direction ($\vec{q}_{1Q}$). (*C*) Topograph showing a *Y*-junction among three such 1Q ribbons, each with a different 1Q CDW direction. The topograph in *A* has been leveled by removing a polynomial background to show the CDW interface clearly. Setpoint parameters: $V_{sample} = -50$ mV, $R_J = 1$ GΩ (*A* and *C*), and 5 GΩ (*B*).
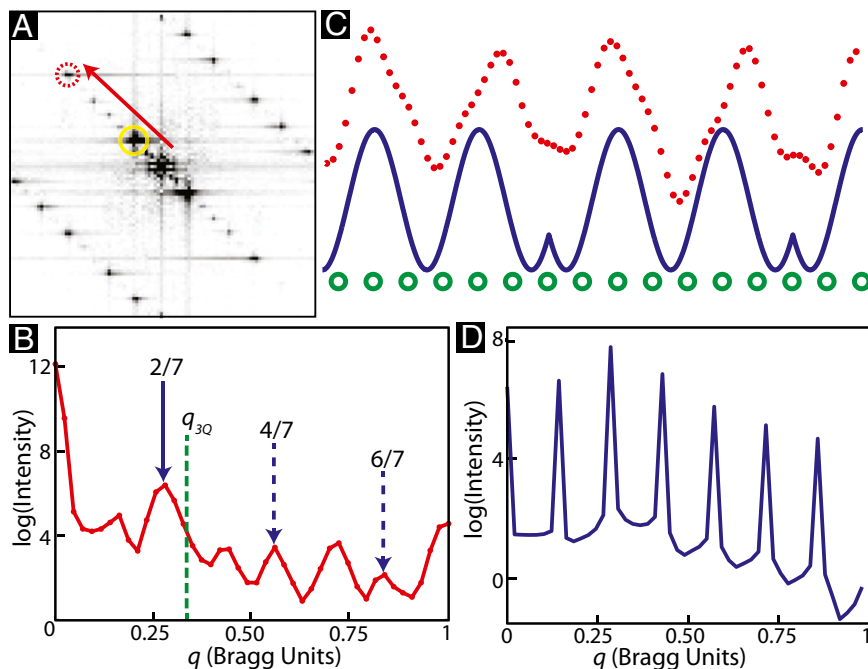
Fig. 3. The 1Q CDW. (*A*) FT of the out-of-feedback current at +50 mV over a 1Q region (upper left quadrant of Fig. 2A). The dominant CDW wavevector (yellow circle) and Bragg vector (dashed red circle) are indicated. (*B*) Linecut of the FT intensity parallel to the red line in *A* from the center to the Bragg peak, in units of the Bragg vector Q_0. The dominant peak, $q_{1Q} \simeq (2/7)Q_0$ (solid blue arrow), and its harmonics (dashed blue arrows) are identified and are distinct from the 3Q wavevector q_{3Q} (dashed green line). The remaining peaks are Bragg reflections of these three peaks. Setpoint parameters: $V_{sample} = -50$ mV and $R_J = 0.2$ GΩ. (*C*) Phenomenological model of the observed 1Q CDW wavelength, $\lambda_{1Q} \simeq 3.5\ a_0$ (details in text). The atomic periodicity is indicated by green circles, and the phase of the CDW order parameter from the model is shown in blue (22). A topographic linecut (red dots) is extracted from Fig. 2A along the red arrow ($\vec{q}_{1Q}$), filtered to remove atomic corrugations and overlaid for comparison. (*D*) Simulated FT intensity from the cartoon CDW modulation in *C*, for comparison with experimental peak positions in *B*.

(Fig. 4) computed from our modeled band structure (*SI Text III*). Therefore, our observations and calculations both indicate that the FS can play only a minor role in determining CDW wavevectors in NbSe₂. This highlights the key role the q-dependence of alternative mechanisms, such as electron–phonon coupling, may play in driving the transition, and particularly the manner in which these mechanisms may be influenced by local strain.

The two CDW regions display quite different tunneling spectra, as shown in Fig. 5 *A* and *B*. We use a fit to the NbSe₂ band
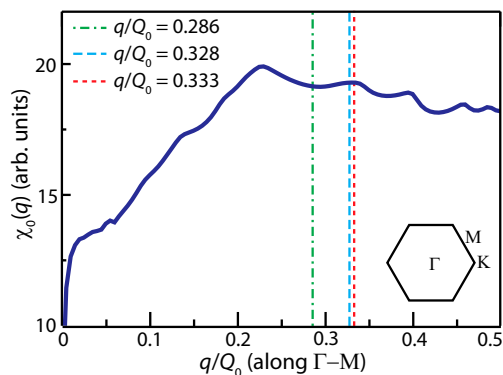
Fig. 4. Susceptibility. The noninteracting susceptibility $\chi_0(q, \omega = 0)$ calculated from a fit to the NbSe₂ band structure (*SI Text III*) along the $\Gamma - M$ direction of the reciprocal lattice, displaying a broad maximum over a range of wavevectors: $\tilde{q} \sim (0.25 - 0.4)Q_0$ (6, 15, 16). The CDW wavevectors q_{1Q}, q_{3Q}, and $Q_0/3$ are overlaid for comparison. (*Inset*) Brillouin zone (BZ) of the hexagonal NbSe₂ lattice.

structure (*SI Text III*) and impose a CDW wavevector $\tilde{q}$, gap $\tilde{\Delta}$, and broadening parameter $\tilde{\Gamma}$ to calculate the density of states (DOS) in Fig. 5C (*SI Text IV*). For the 3Q CDW state, the measured dI/dV spectrum, proportional to the DOS, is reproduced best using $\tilde{q} = (0.333 \pm 0.004)Q_0$ (the observed local CDW periodicity), $\tilde{\Delta} = (12 \pm 2)$ mV (which previously was not apparent from direct observations by spectroscopic techniques), and $\tilde{\Gamma} = 5$ mV. The calculations capture the overall shape, width, and center ε_{min} of the gap structure within 30 mV of ε_F (*SI Text IV*). The fact that ε_{min} is offset from ε_F should be unsurprising for a quasi-2D system (26), but had not been understood or observed in NbSe₂ until now because of the limitations of spectroscopic techniques, which are sensitive to filled states only (13).

We disentangle the CDW gap from other effects in the 3Q spectra through a comparison with the 1Q spectra in Fig. 5B. These V-shaped 1Q spectra resemble the linear tunneling conductance background historically attributed to the inelastic coupling of tunneling electrons to a flat bosonic spectrum (27). That this background is much stronger in the 1Q region, obscuring band structure effects, likely is a strain-induced phenomenon, which may be related to the buckling and associated decoupling of the topmost layers in the 1Q region. Meanwhile, present in both 1Q and 3Q spectra (thus, unlikely to be associated with these different CDWs), yet absent in calculations (thus, unlikely to be a band structure effect), are the ±35 mV kinks, previously and mistakenly identified as the CDW gap (21). We universally observe the kinks even well above T_{CDW}, which further demonstrates their lack of bearing on the CDW phase (*SI Text IV*). ARPES studies observe a prominent band structure kink at a similar energy in the Se Γ-pocket (16, 19), attributed to coupling to an optical phonon (14). Therefore, we conclude that this self-energy effect is responsible for the ε_K-kinks in the tunneling spectra as well. The discrepancy between the data
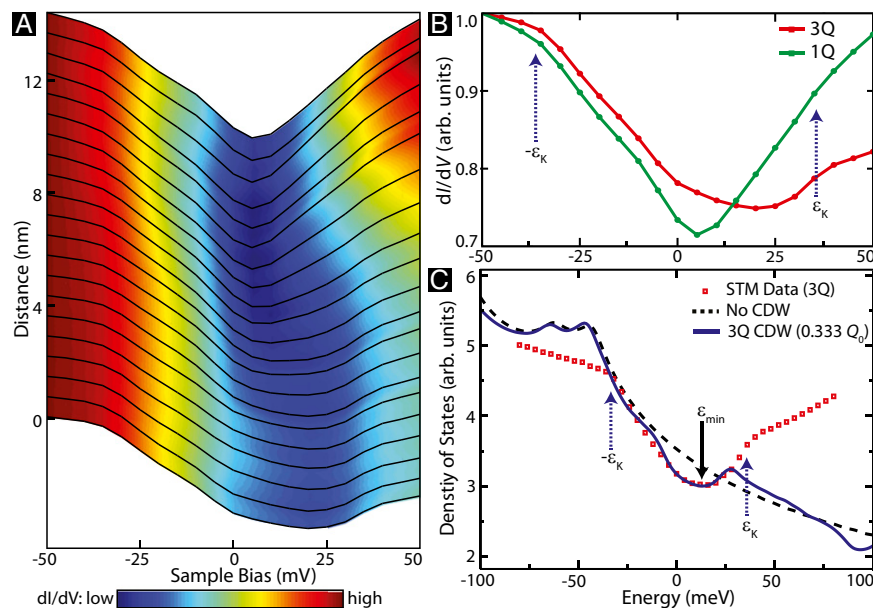
Fig. 5. Spectroscopy across the 1Q–3Q interface. (*A*) Linecut of *dI/dV* spectra across the 1Q–3Q interface taken along the red arrow in Fig. 2*A*. (*B*) Representative spectra in the 3Q (red) and 1Q (green) regions of Fig. 2*A* are overlaid for comparison. The 1Q spectra have a minimum close to ε_F, a deep *V*-shape with reduced asymmetry, and kinks at $\pm\varepsilon_K$. The spectra are normalized at –50 mV. Setpoint parameters: V_{sample} = –50 mV, R_J = 0.2 GΩ, and V_{rms} = 3.5 mV. (*C*) Calculated DOS for NbSe$_2$ in the "normal" state (black) and in the presence of a 3Q CDW (blue) using $\tilde{q}$ = 0.333Q_0, $\tilde{\Delta}$ = 12 mV, compared with the 3Q STM spectrum (red) (details in *SI Text IV*). The calculations reproduce the observed asymmetry, offset ε_{min}, and shape of the gap structure.

and band structure calculations above ∼30 mV in Fig. 5*C* thus may be attributed to the inelastic tunneling background and self-energy effects.

Discussion

We therefore resolve a longstanding debate about the anomalous CDW gap magnitude reported by STM measurements (21), and caution that not all ε_F-symmetric kinks in tunneling spectra are associated with order (e.g., density wave or superconducting gaps). On the contrary, we emphasize that the true CDW signature in NbSe$_2$ is offset from ε_F, which has confused an active research community for two decades, and has been disentangled now only by a combination of spatially resolved filled- and empty-state spectroscopy of a proximate (1Q) phase and band structure calculations (26). This emphasizes the need for full experimental exploration of proximate phases in other pertinent materials, combined with quantitative modeling. We further suggest that controlled local strain, through epitaxy or intentional defects, may be a useful tuning parameter to access the necessary proximate phases for comparison.

Beyond providing unique insight into the nature of the 3Q CDW in NbSe$_2$, our work motivates the utility of the 1Q–3Q interface in NbSe$_2$ as a platform to explore competing quantum phases in the weakly correlated limit, as a step toward understanding them in strongly correlated systems. In the Landau picture of CDWs (25), a quantum phase transition between 3Q and 1Q states may arise by tuning the coefficient of the interaction term among the three inequivalent CDW propagation directions (although in our case, the magnitude of q differs between the two states). In NbSe$_2$, even at low temperatures $T \ll T_{CDW}$, where the amplitude of the order parameter is already large, moderate strain is seen to have a strong influence, indicating that the system is intrinsically close to the QCP separating these states. We note that a related phase transition between the observed 1Q CDW phase and a "hidden" 2Q phase has been suggested, but not directly visualized, in the rare-earth tritellurides (28, 29).

Our discovery provides a unique perspective on the role of density wave order in complex systems. First, our resolution of

two longstanding debates about NbSe$_2$ puts this much-studied material on firmer footing as a well-understood model system for CDW studies and competing ground states in superconductors. We have disentangled the true CDW gap, and clarified that FS nesting plays a minor role in determining the CDW wavevectors in this material, thereby highlighting the role of other mechanisms in driving the transition. Second, our revelation of a particle-hole asymmetric CDW gap emphasizes the limitations of filled-state-only probes, e.g., ARPES, for investigating phases other than SC—which is unambiguously particle-hole symmetric. Full spectral probes such as STM, in combination with quantitative calculations, are necessary to understand the competition between SC and particle-hole asymmetric phases. Third, our observation of the local effect of even moderate strain in driving a quantum phase transition calls for a reinvestigation of possible phase inhomogeneity in other strongly correlated systems, in which larger strain may occur (30, 31).

In the cuprate superconductors, an analogous phase boundary between unidirectional (1Q) charge "stripes" and bidirectional (2Q) "checkerboard" has been predicted (32, 33). The introduction of quenched disorder results in discommensurations in the 2Q phase and disordered orientational order in the 1Q phase, making them hard to distinguish—especially in the cuprate superconductors, thought to be in proximity to the 1Q–2Q phase boundary (32, 33). Recent STM studies of the ∼4 a_0 charge order in the cuprate Bi$_2$Sr$_2$Ca$_{n-1}$Cu$_n$O$_{2n+4+x}$ (BSCCO) have had conflicting interpretations, with independent suggestions of fluctuating 2Q and 1Q order (34, 35). However, the influence of strain, from the supermodulation lattice buckling or from randomly distributed dopants, is seldom accounted for. Previous studies have shown that both these strain phenomena correlate with nanoscale electronic inhomogeneity (30, 36). A possible explanation is local stabilization of the 1Q state, producing 1Q–2Q and 1Q–1Q interfaces with spectral differences, analogous to Figs. 2 and 5 *A* and *B*. Although the presence of strong disorder [up to 12% strain variations on a nanometer length scale (30)] complicates the interpretations in BSCCO, we stress the importance of isolating and modeling strain effects for better

understanding and control of the phase transitions in cuprates. Finally, the microscopic visualization of the role of strain in stabilizing new order suggests a controlled route toward engineering novel quantum phases and interfaces and studying symmetry breaking in strongly correlated materials. In this regard, we suggest a connection to the emerging importance of strain as a route to high-T_c superconductivity in novel iron-based materials (37, 38).

Materials and Methods

STM Experiments. Measurements were performed using a home-built STM at temperatures between 2 K and 10 K. Magnetic fields of up to 6 T were used to suppress the superconducting state as needed. Single crystals of $2H$-NbSe$_2$ were cleaved in situ in cryogenic ultrahigh vacuum and inserted into the STM. A mechanically cut Pt-Ir tip, cleaned by field emission and characterized on gold, was used for the measurements. Spectroscopy data were acquired using a lock-in technique at 1.115 kHz. The topographic and spectroscopic signatures of the 1Q ribbons have been verified with several tips.

Band Structure and DOS Calculations. The band structure of $2H$-NbSe$_2$ close to ε_F consists of two Nb-4d–derived bands and one Se-4p "pancake"-shaped hole pocket (6). The Nb-4d bands are modeled using a tight-binding fit to the observed ARPES band structure (16), and the Se-4p pocket is approximated by a simple quadratic form to fit first principles calculations (6) (details in *SI Text III*). Using all three bands, the DOS in the presence of a CDW is calculated by imposing a constant coupling between electronic states connected by any one of the three q-vectors. The strength of the coupling $\tilde{\Delta}$ is taken as a free parameter in the reproduction of the experimentally observed DOS, and the size of $\tilde{q}$ is allowed to vary slightly around the observed value of 0.328 Q_0 (details in *SI Text IV*).

1. Sachdev S (2000) Quantum criticality: Competing ground states in low dimensions. *Science* 288(5465):475–480.
2. Norman MR, Pines D, Kallin C (2005) The pseudogap: Friend or foe of high T_c? *Adv Phys* 54(8):715–733.
3. Johnston DC (2010) The puzzle of high temperature superconductivity in layered iron pnictides and chalcogenides. *Adv Phys* 59(6):803–1061.
4. Jérome D, Schulz HJ (2002) Organic conductors and superconductors. *Adv Phys* 51(1):293–479.
5. Kivelson SA, et al. (2003) How to detect fluctuating stripes in the high-temperature superconductors. *Rev Mod Phys* 75(4):1201–1241.
6. Johannes MD, Mazin II, Howells CA (2006) Fermi-surface nesting and the origin of the charge-density wave in NbSe$_2$. *Phys Rev B* 73(20):205102.
7. Varma CM, Simons AL (1981) Strong-coupling theory of charge-density-wave transitions. *Phys Rev Lett* 51(2):138–141.
8. Suderow H, Tissen VG, Brison JP, Martínez JL, Vieira S (2005) Pressure induced effects on the Fermi surface of superconducting $2H$-NbSe$_2$. *Phys Rev Lett* 95(11):117006.
9. Kiss T, et al. (2007) Charge-order-maximized momentum-dependent superconductivity. *Nat Phys* 3(10):720–725.
10. Feng Y, et al. (2012) Order parameter fluctuations at a buried quantum critical point. *Proc Natl Acad Sci USA* 109(19):7224–7229.
11. Moncton DE, Axe JD, DiSalvo FJ (1975) Study of superlattice formation in $2H$-NbSe$_2$ and $2H$-TaSe$_2$ by neutron scattering. *Phys Rev Lett* 34(12):734–737.
12. Wilson JA, Salvo FJD, Mahajan S (2001) Charge-density waves and superlattices in the metallic layered transition metal dichalcogenides. *Adv Phys* 50(8):1171–1248.
13. Borisenko SV, et al. (2009) Two energy gaps and Fermi-surface "arcs" in NbSe$_2$. *Phys Rev Lett* 102(16):166402.
14. Mialitsin A (2010) Raman scattering from layered superconductors: Effects of charge ordering, two-band superconductivity, and structural disorder. PhD thesis (Rutgers University, New Brunswick, NJ).
15. Weber F, et al. (2011) Extended phonon collapse and the origin of the charge-density wave in $2H$-NbSe$_2$. *Phys Rev Lett* 107(10):107403.
16. Rahn DJ, et al. (2012) Gaps and kinks in the electronic structure of the superconductor $2H$-NbSe$_2$ from angle-resolved photoemission at 1 K. *Phys Rev B* 85(22):224532.
17. Straub T, et al. (1999) Charge-density-wave mechanism in $2H$-NbSe$_2$: Photoemission results. *Phys Rev Lett* 82(22):4504–4507.
18. Rossnagel K, et al. (2001) Fermi surface of $2H$-NbSe$_2$ and its implications on the charge-density-wave mechanism. *Phys Rev B* 64(23):235119.
19. Valla T, et al. (2004) Quasiparticle spectra, charge-density waves, superconductivity, and electron-phonon coupling in $2H$-NbSe$_2$. *Phys Rev Lett* 92(8):086401.
20. Shen DW, et al. (2008) Primary role of the barely occupied states in the charge density wave formation of NbSe$_2$. *Phys Rev Lett* 101(22):226406.
21. Hess HF, Robinson RB, Waszczak JV (1991) STM spectroscopy of vortex cores and the flux lattice. *Physica B* 169(1-4):422–431.
22. McMillan WL (1976) Theory of discommensurations and the commensurate-incommensurate charge-density-wave phase transition. *Phys Rev B* 14(4):1496–1502.
23. Wang H, Lee J, Dreyer M, Barker BI (2009) A scanning tunneling microscopy study of a new superstructure around defects created by tip-sample interaction on $2H$-NbSe$_2$. *J Phys Condens Matter* 21(26):265005.
24. Bando H, Miyahara Y, Enomoto H, Ozaki H (1997) Scanning tunneling microscopy investigations of single-q charge density wave state in hafnium-doped tantalum disulfide. *Surf Sci* 381(2-3):L609–L613.
25. McMillan WL (1975) Landau theory of charge-density waves in transition-metal dichalcogenides. *Phys Rev B* 12(4):1187–1196.
26. Norman MR, Kanigel A, Randeria M, Chatterjee U, Campuzano JC (2007) Modeling the Fermi arc in underdoped cuprates. *Phys Rev B* 76(17):174501.
27. Kirtley JR, Washburn S, Scalapino DJ (1992) Origin of the linear tunneling conductance background. *Phys Rev B Condens Matter* 45(1):336–346.
28. Yao H, Robertson JA, Kim EA, Kivelson SA (2006) Theory of stripes in quasi-two-dimensional rare-earth tellurides. *Phys Rev B* 74(24):245120.
29. Ru N, et al. (2008) Effect of chemical pressure on the charge density wave transition in rare-earth tritellurides RTe$_3$. *Phys Rev B* 77(3):035114.
30. Slezak JA, et al. (2008) Imaging the impact on cuprate superconductivity of varying the interatomic distances within individual crystal unit cells. *Proc Natl Acad Sci USA* 105(9):3203–3208.
31. Chu JH, et al. (2010) In-plane resistivity anisotropy in an underdoped iron arsenide superconductor. *Science* 329(5993):824–826.
32. Robertson JA, Kivelson SA, Fradkin E, Fang AC, Kapitulnik A (2006) Distinguishing patterns of charge order: Stripes or checkerboards. *Phys Rev B* 74(13):134507.
33. Del Maestro A, Rosenow B, Sachdev S (2006) From stripe to checkerboard ordering of charge-density waves on the square lattice in the presence of quenched disorder. *Phys Rev B* 74(2):024520.
34. Wise WD, et al. (2008) Charge-density-wave origin of cuprate checkerboard visualized by scanning tunnelling microscopy. *Nat Phys* 4(9):696–699.
35. Parker CV, et al. (2010) Fluctuating stripes at the onset of the pseudogap in the high-T_c superconductor Bi$_2$Sr$_2$CaCu$_2$O$_{8+x}$. *Nature* 468(7324):677–680.
36. Zeljkovic I, et al. (2012) Imaging the impact of single oxygen atoms on superconducting Bi$_{2+y}$Sr$_{2-y}$CaCu$_2$O$_{8+x}$. *Science* 337(6092):320–323.
37. Saha SR, et al. (2012) Structural collapse and superconductivity in rare-earth-doped CaFe$_2$As$_2$. *Phys Rev B* 85(2):024525.
38. Wang QY, et al. (2012) Interface-induced high-temperature superconductivity in single unit-cell FeSe films on SrTiO$_3$. *Chin Phys Lett* 29(3):037402.

PHYSICS

Supporting Information

Soumyanarayanan et al. 10.1073/pnas.1211387110

SI Text

Sample Characterization. NbSe$_2$ is a layered transition metal dichalcogenide whose 2H polytype has a hexagonal structure and D_{6h}^4 space group symmetry. The unit cell (Fig. S1A) consists of two sandwiches of Se–Nb–Se. The crystal typically cleaves between the neighboring Se layers, coupled by weak van der Waals forces.

Single crystals of 2H-NbSe$_2$ were grown by chemical vapor transport using iodine as the transport agent. A transport characterization of the sample batch used in this work is shown in Fig. S1B. The superconducting transition is observed at $T_{SC} \sim 7$ K. The residual resistivity ratio, defined as the ratio of resistances $R(295\text{K})/R(7.5\text{K})$, is ~16.

1Q Ribbons: Height and Orientation. The 1Q charge-density wave (CDW) typically appears in regions that persist in one direction with apparent 20–40 pm topographic elevation, forming a 10–20-nm wide ribbon structure (Fig. S2 A–C). We note that the topographic elevation $z_{STM}(\vec{r}, V_0, I_0)$ as measured by maintaining a constant current I_0 with bias setpoint V_0 at lateral tip position $\vec{r} \equiv (x, y)$ may be given by:

$$z_{STM}(\vec{r}, V_0, I_0) \simeq z_T(\vec{r}) + \frac{1}{\kappa(\vec{r})} \cdot \ln \left(\frac{I_0}{\int_0^{V_0} dV e D(\vec{r}, eV))} \right). \quad \text{[S1]}$$

Here $z_T(\vec{r})$ is the true topographic corrugation of the sample, $\kappa(\vec{r})$ is a measure of the local tunnel barrier height, and $D(\vec{r}, eV)$ is the local density of states (LDOS) of the sample at energy eV. Because of the logarithmic sensitivity of $z_{STM}(\vec{r}, V_0, I_0)$ to the integral of the LDOS from the Fermi energy, ε_F (corresponding to $V = 0$) up to the bias setpoint eV_0, scanning tunneling microscopy (STM) topographs may contain electronic artifacts masquerading as geometric effects. Therefore, we present two pieces of evidence for the true geometric elevation of these ribbons.

First, a tabulation of the relative orientation θ_{R,Q_0} of the ribbon to the nearest Bragg vector of the underlying hexagonal lattice for the various ribbons imaged in the study shows a seemingly random spread from −30° to 30°—the full range of available angles (Fig. S2 D and E). Furthermore, these ribbon structures may intersect to form X- as well as Y-junctions (Fig. S2 A and B), and the angle between intersecting ribbons varies from 40° to 60°. The fact that ribbon orientation does not respect lattice symmetry strongly suggests a true geometric rather than an electronic origin of their apparent height. We contrast this observation with enhanced STM topographic corrugation associated with predominantly electronic features in a wide range of other materials, which respect the symmetry of the hexagonal (1, 2) or square (3) lattice.

Second, the measured height of these ribbons in STM topographs exhibits <5% dependence on bias setpoint within 400 mV below the Fermi energy (Fig. S3 A–C). We note that this energy range over which the measured height of the ribbons is invariant is much larger than the spectral range of CDW variation (~50 mV). We further note the contrast between the bias-independent ribbons and single-atom impurity resonances, whose measured "height" varies by 50–70% between Fig. S3A and S3B. Therefore, we conclude that the measured height (20–40 pm) and width (10–20 nm) of these ribbons has a predominantly geometric origin.

Having established the topographic origin of these ribbons (Figs. S2 and S3), we suggest that these ribbons likely are a topographic rippling of the top few layers. These ribbons may arise during the cleaving process as the result of underlying growth defects that may intercalate between Se–Nb–Se sandwich layers. We note that similar topographic ribbon deformations were observed recently in another layered chalcogenide (Bi$_2$Te$_3$) (4).

We estimate the in-plane and out-of-plane lattice strain associated with the topographic ribbon features. Using the maximum topographic elevation of an observed ribbon (40 pm), we can put an upper limit on the out-of-plane distortion by assuming that a minimum of two sandwich layers are elevated (any fewer and the defects causing the elevation likely would be visible in our topographs). The out-of-plane distortion therefore is ≲3% (40 pm/ 12.54 Å) of the unit cell spacing. To measure the in-plane distortion, we first use the Lawler-Fujita algorithm (5), which can determine the lateral location of atoms with precision ~2% of the lattice spacing (6, 7). With this algorithm, we do not observe any change in the lattice constant across the ribbon, which places a direct experimental upper limit on the in-plane distortion of ~2%.

However, we can estimate the actual in-plane distortion indirectly from the measured out-of-plane distortion by modeling the ribbon as a half-period of a sinusoid with height h (40 pm) and width W (10 nm) (Fig. S3D). The total lateral deformation due to such a ribbon is $\delta W \sim 45$ pm, corresponding to ~0.06% of the lattice spacing. As this is well below the resolution of the Lawler-Fujita algorithm, it is not surprising that the in-plane distortion is not detectable in STM topographs. From the upper bounds of 3% on the vertical strain and 0.06% on the lateral strain, we note that the magnitude of the strain field leading to the formation of these ribbons is moderate compared with some other correlated materials (8, 9). We also note that although the magnitude of lattice distortion of these ribbons may seem small in the context of the observed quantum phase inhomogeneity, a comparison with other known materials suggests that strain of this magnitude may be sufficient to drive a transition to the unidirectional CDW phase (10).

Previously, we discussed the ribbon orientation with respect to the lattice (θ_{R,Q_0}); we now consider the ribbon orientation with respect to the 1Q CDW wavevector $(\theta_{R,q_{1Q}})$, also detailed in Fig. S2 D and E. In a simple picture of the strained ribbon structure, we would expect the ribbon-induced strain to couple strongly to the 1Q CDW orientation either parallel or perpendicular to the ribbon; thus, we would expect to observe values of $\theta_{R,q_{1Q}}$ either between 0° and 30° or between 60° and 90°. However, we often find $\theta_{R,q_{1Q}}$ to be in the 30–60° range as well. Insufficient statistics prevent us from inferring a clear connection between ribbon orientation and $\vec{q}_{1Q}$ orientation, but the wide distribution of relative angles suggests the complexity of the interaction.

Band Structure Calculations. The band structure of 2H-NbSe$_2$ close to ε_F consists of two Nb-4d-derived bands and one Se-4p "pancake"-shaped hole pocket (11, 12). Close to ε_F, the Se-4p pancake-shaped hole pocket that surrounds the Γ-point can be modeled by a simple quadratic form:

$$E = A \cdot \frac{a_0^2}{4\pi^2} \left(k_x^2 + k_y^2 \right) + B. \quad \text{[S2]}$$

With the values of $A = -5.4$ eV and $B = -0.65$ eV, this model accurately reproduces the dispersion obtained in first principles local density approximation (LDA) calculations by Johannes et al. (11), as shown in Fig. S4A. To model the Nb-4d bands, we use a tight-binding fit to the band structure observed in angle-resolved photoemission (ARPES) experiments, as reported by Rahn et al.

(13). We find that a small ($\sim +16$ meV) offset in the chemical potential relative to the parameters used by Rahn et al. was needed to reproduce the observed DOS from STM measurements. This offset is within the accuracy of the tight-binding fitting scheme (13). The band energies of the tight-binding description are given by (13)

$$\begin{aligned} E = \; & t_0 + t_1[2 \cos \xi \cos \eta + \cos 2\xi] \\ & + t_2[2 \cos 3\xi \cos \eta + \cos 2\eta] \\ & + t_3[2\cos2\xi\cos2\eta + \cos 4\xi] \\ & + t_4[\cos \xi \cos 3\eta + \cos 5\xi \cos \eta + \cos 4\xi \cos 2\eta] \\ & + t_5[2 \cos 3\xi \cos3\eta + \cos 6\xi], \end{aligned} \qquad \textbf{[S3]}$$

where $\xi = \frac{1}{2}k_x a$ and $\eta = \frac{1}{2}\sqrt{3}k_y a$ and k_y is along $\Gamma - M$. The values of the tight-binding parameters (including the offset) used in this work are presented in Table S1.

Density of States Calculations. To calculate the DOS in the presence of a 3Q CDW, we impose a coupling between states connected by any one of the three $\tilde{q}$-vectors, given by

$$\mathcal{H}_{\mathrm{CDW}} = \tilde{\Delta} \cdot \sum_{\vec{k}} \left(c_{\vec{k}+\tilde{q}}^{\dagger} \, c_{\vec{k}} + \mathrm{h.c.} \right). \qquad \textbf{[S4]}$$

The strength $\tilde{\Delta}$ of the coupling is taken as a free parameter in the reproduction of the experimentally observed DOS, with a broadening parameter fixed at $\Gamma = 5$ meV. Adjusting the size of $\tilde{q}$ slightly around the observed value of $q_{3Q} = 0.328 \, Q_0$, we find the best match with STM spectra using $\tilde{q} = 0.333 \, Q_0$ (corresponding to the locally commensurate CDW periodicity), $\tilde{\Delta} = 12$ meV. With these parameter values, the gap structure in the calculated DOS closely approaches the overall shape, width, and center of the gap structure seen in the measured data within ± 30 meV of the Fermi energy ε_{F}, as shown in Fig. 5C.

To demonstrate the accuracy of this fit, we show the effects of varying the wavevector $\tilde{q}$ by $1 - 2\%$ (Fig. S5 A and B), and the gap value $\tilde{\Delta}$ by $10 - 20\%$ (Fig. S5 C and D). Using these fit parameter variations, we estimate the errors for $\tilde{q}$ and $\tilde{\Delta}$ to be $0.004 \, Q_0$ and 2 meV, respectively. The value of $\tilde{\Delta}$, however, may be an overestimate, leading to a systematic error of the same order as the fit uncertainty, because the described procedure does not take into account the particle-hole symmetric

inelastic background in the experimental DOS. Accurate modeling of the inelastic background would require detailed temperature-dependent spectroscopic data, which is beyond the scope of this work.

Crucially, we note that the particle-hole asymmetry in the CDW gap, with its minimum centered above ε_{F}, cannot be removed by the subtraction of a particle-hole symmetric background. Likewise, the striking deviation of our fitted gap parameter ($\tilde{\Delta} = 12$ meV) from previous results [four times larger than the 3 meV value detailed by Borisenko et al. (14) and three times smaller than the 35 meV value detailed by Hess et al. (15)] far exceeds fit or systematic uncertainties.

To experimentally verify the lack of bearing of the 35 mV kinks on the CDW phase, we performed spectroscopy up to 45 K, and universally observed the presence of these kinks in the STM spectra well above T_{CDW} (~ 33 K). A comparison of the typical spectrum acquired at 40 K with that acquired at 2 K is shown in Fig. S6. We note that the data acquired at 40 K are thermally smeared by $\mathcal{O}(3k_B T)$, i.e., ~ 10 mV, resulting in a broadening of the kinks. Despite this, the kinks remain distinguishable and are present throughout all spatial regions studied in this work.

For completeness, we show in Fig. S7A the calculated DOS in the presence of a 1Q CDW at the experimentally observed wavevector, $q_{1Q} = 0.286 \, Q_0$, using $\tilde{\Delta} = 12$ meV. The lack of correspondence between this calculation (green curve in Fig. S7A) and the measured dI/dV spectrum (green curve in Fig. 5B) may be attributed to the increased intensity of the inelastic background in the buckled region of the 1Q ribbons. This background is evident in the V-shape of the dI/dV spectrum in Fig. 5B, centered close to ε_{F}, as explained theoretically (16) and observed experimentally across a wide variety of materials (16–23).

We also compare our results with a calculation of the DOS based on a tight-binding fit to the full 3D LDA band structure reported by Johannes et al. (11). The DOS obtained using this 3D LDA fit is compared with the results based on the 2D fit in Fig. S7B. We find that the STM data are best reproduced using the band structure observed by ARPES, and that there is a noticeable difference between the depths of the gaps in the 2D ARPES-based and those of the 3D LDA-based band structure fits (despite independent parameter optimization), which is indicative of some difference between the surface and bulk dispersions (11).

1. Hanaguri T, Igarashi K, Kawamura M, Takagi H, Sasagawa T (2010) Momentum-resolved Landau-level spectroscopy of Dirac surface state in Bi$_2$Se$_3$. *Phys Rev B* 82(8):081305.
2. Rutter GM, et al. (2007) Scattering and interference in epitaxial graphene. *Science* 317 (5835):219–222.
3. Wise WD, et al. (2008) Charge-density-wave origin of cuprate checkerboard visualized by scanning tunnelling microscopy. *Nat Phys* 4(9):696–699.
4. Okada Y, (2012) Ripple-modulated electronic structure of a 3D topological insulator. *Nat Commun* 3:1158.
5. Lawler MJ, et al. (2010) Intra-unit-cell electronic nematicity of the high-T(c) copper-oxide pseudogap states. *Nature* 466(7304):347–351.
6. Hamidian MH, et al. (2012) Picometer registration of zinc impurity states in Bi$_2$Sr$_2$CaCu$_2$O$_{8+\delta}$ for phase determination in intra-unit-cell Fourier transform STM. *New J Phys* 14(5):053017.
7. Williams TL (2011) Nanoscale Electronic Structure of Cuprate Superconductors Investigated with Scanning Tunneling Spectroscopy. PhD thesis (Harvard Univ., Cambridge, MA).
8. Slezak JA, et al. (2008) Imaging the impact on cuprate superconductivity of varying the interatomic distances within individual crystal unit cells. *Proc Natl Acad Sci USA* 105(9):3203–3208.
9. Chu JH, et al. (2010) In-plane resistivity anisotropy in an underdoped iron arsenide superconductor. *Science* 329(5993):824–826.
10. Ru N, et al. (2008) Effect of chemical pressure on the charge density wave transition in rare-earth tritellurides RTe$_3$. *Phys Rev B* 77(3):035114.
11. Johannes MD, Mazin II, Howells CA (2006) Fermi-surface nesting and the origin of the charge-density wave in NbSe$_2$. *Phys Rev B* 73(20):205102.

12. Rossnagel K, et al. (2001) Fermi surface of 2H-NbSe$_2$ and its implications on the charge-density-wave mechanism. *Phys Rev B* 64(23):235119.
13. Rahn DJ, et al. (2012) Gaps and kinks in the electronic structure of the superconductor 2H-NbSe$_2$ from angle-resolved photoemission at 1 K. *Phys Rev B* 85(22):224532.
14. Borisenko SV, et al. (2009) Two energy gaps and Fermi-surface "arcs" in NbSe$_2$. *Phys Rev Lett* 102(16):166402.
15. Hess HF, Robinson RB, Waszczak JV (1991) STM spectroscopy of vortex cores and the flux lattice. *Physica B* 169(1-4):422–431.
16. Kirtley JR, Washburn S, Scalapino DJ (1992) Origin of the linear tunneling conductance background. *Phys Rev B Condens Matter* 45(1):336–346.
17. Kirtley JR, Scalapino DJ (1990) Inelastic-tunneling model for the linear conductance background in the high-Tc superconductors. *Phys Rev Lett* 65(6):798–800.
18. Niestemski FC, et al. (2007) A distinct bosonic mode in an electron-doped high-transition-temperature superconductor. *Nature* 450(7172):1058–1061.
19. Fridman I, Yeh KW, Wu MK, Wei JYT (2011) STM spectroscopy on superconducting FeSe$_{1-x}$Te$_x$ single crystals at 300 mK. *J Phys Chem Solids* 72(5):483–485.
20. Arai T, et al. (2001) Tunneling spectroscopy on the organic superconductor κ-(BEDT-TTF)$_2$Cu(NCS)$_2$ using STM. *Phys Rev B* 63(10):104518.
21. Rahnejat KC, et al. (2011) Charge density waves in the graphene sheets of the superconductor CaC$_6$. *Nat Commun* 2:558.
22. Collins RT, Lambe J, McGill TC, Burnham RD (1984) Inelastic tunneling characteristics of AlAs/GaAs heterojunctions. *Appl Phys Lett* 44(5):532–534.
23. McMillan W, Mochel J (1981) Electron tunneling experiments on amorphous Ge$_{1-x}$Au$_x$. *Phys Rev Lett* 46(8):556–557.
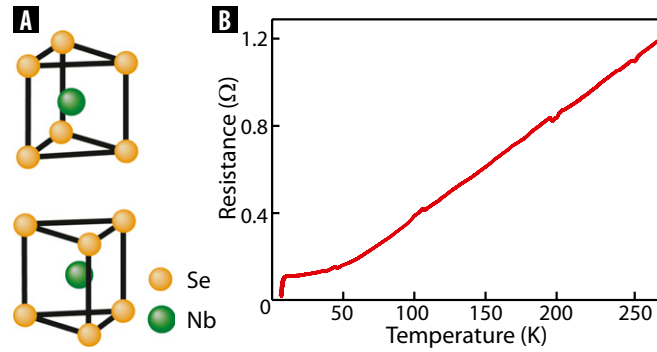
Fig. S1. Sample characterization. (*A*) The layered hexagonal crystal structure of 2*H*-NbSe$_2$, with alternating sandwiches of Se–Nb–Se. (*B*) Temperature dependence of the resistance for the sample batch used for this study, showing a superconducting transition at ∼7 K.
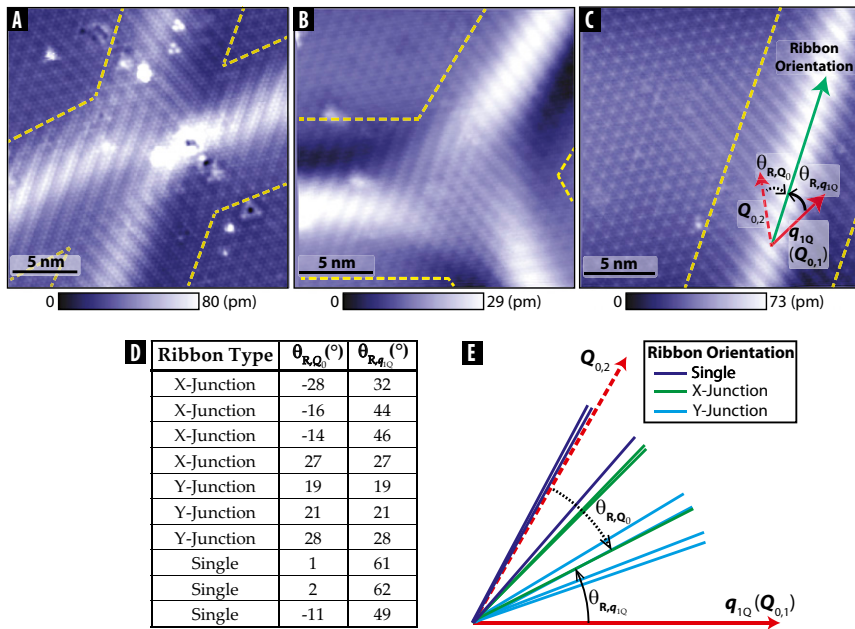

Ribbon Type	θ_{R,Q_0}(°)	$\theta_{R,q_{1Q}}$(°)
X-Junction	-28	32
X-Junction	-16	44
X-Junction	-14	46
X-Junction	27	27
Y-Junction	19	19
Y-Junction	21	21
Y-Junction	28	28
Single	1	61
Single	2	62
Single	-11	49

Fig. S2. 1*Q* ribbons: orientation. (*A* and *B*) STM topographs showing ribbons of unidirectional (1*Q*) CDW, intersecting to form an *X*-junction (*A*) and a *Y*-junction (*B*), with CDW wavevector $\vec{q}_{1Q}$ varying between the arms. Dashed yellow lines indicate the approximate extent of the ribbons. Setpoint parameters: $V_{sample} = -50$ mV for both; $R_J = 5$ GΩ(*A*), 1 GΩ(*B*). (*C*) STM topograph of a 1*Q* − 3*Q* interface (top arm of *X*-junction, also shown in Fig. 2*B*), demonstrating the definitions of the relative orientations θ_{R,Q_0} between the ribbon (green arrow) and the nearest Bragg vector (dashed red arrow), and $\theta_{R,q_{1Q}}$, between the ribbon and 1*Q* wavevector $\vec{q}_{1Q}$ (solid red arrow). (*D*) Table detailing the values of θ_{R,Q_0} and $\theta_{R,q_{1Q}}$ observed in the various 1*Q* ribbons studied in this work, with the first entry corresponding to *C*. (*E*) Illustration of the spread of values in *D*. The dark blue (single), green (*X*-junction), and cyan (*Y*-junction) lines describe the orientation of the various ribbons with respect to the 1*Q* wavevector $\vec{q}_{1Q}$ along the $\vec{Q}_{0,1}$ Bragg vector (solid red arrow) and another Bragg vector $\vec{Q}_{0,2}$ (dashed red arrow).
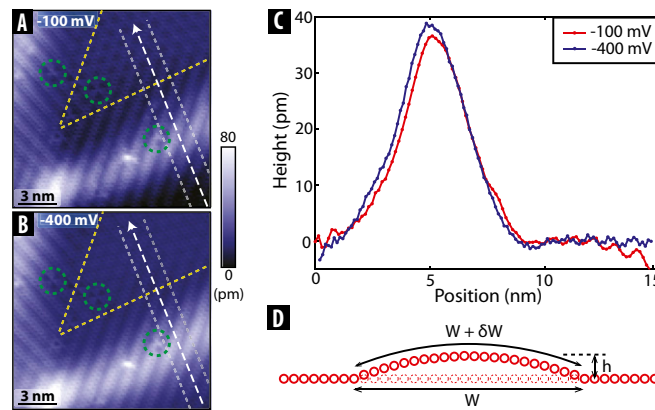
Fig. S3. 1*Q* ribbons: bias setpoint dependence. (*A* and *B*) Topographs of 1*Q* ribbons over the same spatial area acquired with different bias setpoints: −100 mV (*A*) and −400 mV (*B*), with R_J = 10 GΩ in both. The dashed yellow lines indicate the approximate extent of the ribbons, and the dashed green circles enclose triangular impurities, visible in *B* with a 50–70% larger apparent height than in *A*. (*C*) Linecuts taken through the topographs in *A* (red) and *B* (blue) transverse to the lower ribbon, along the dashed white arrows. The measured ribbon height varies less than 5% between bias setpoints −100 mV and −400 mV. The linecuts have been averaged laterally over a 3-nm width, indicated by the dashed gray lines. (*D*) A cartoon representation of the lattice distortion caused by the formation of such a ribbon, modeled as a half-period of a sinusoid. The red circles correspond to rows of displaced Se atoms, whereas the dashed red circles represent their original undistorted positions. The ribbon has height *h* (40 pm) and width *W* (10 nm), resulting in a total lateral distortion of $\delta W \sim 45$ pm across the ribbon.
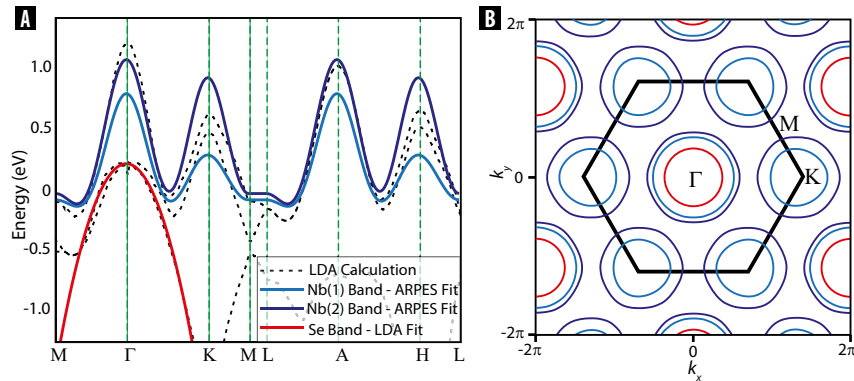

Fig. S4. Band structure calculations. (*A*) Calculated band structure of 2*H*-NbSe$_2$ along high-symmetry directions, showing the two Nb-4*d* bands obtained using an ARPES tight-binding fit (13), and the Se-4*p* band, modeled as a parabolic fit to LDA calculations of Johannes et al. (11), compared with the LDA calculations (dashed black lines). (*B*) Fermi surface obtained using this band structure fit, with the BZ shown in black.
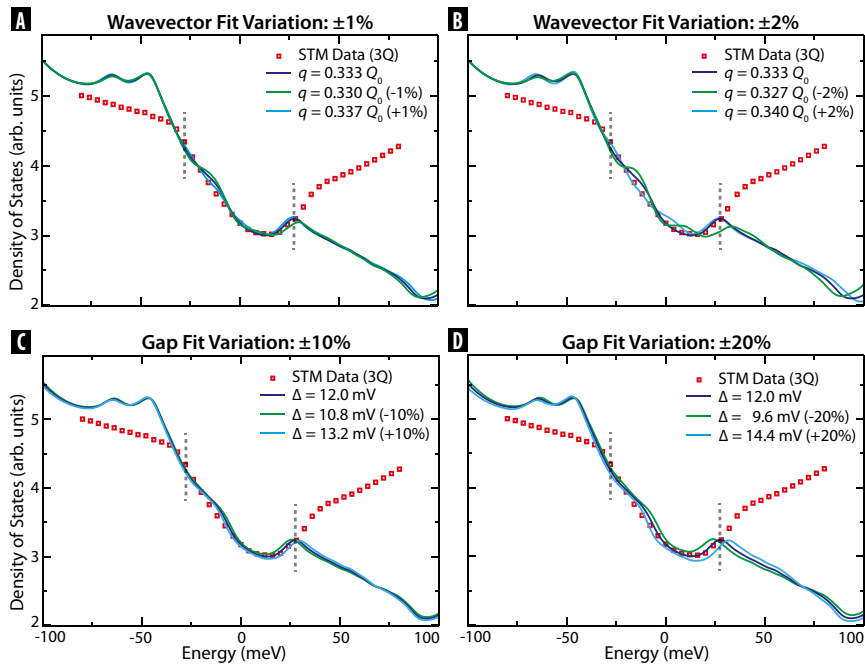
Fig. S5. Variations in DOS fit parameters. Calculated DOS spectrum using the band structure fit in the presence of a 3Q CDW, showing the effects of varying the fit parameters, wavevector $\tilde{q}$, and gap value $\tilde{\Delta}$ around the best-fit values ($\tilde{q} = 0.333\ Q_0$, $\tilde{\Delta} = 12$ meV, dark blue), compared with the STM data (red). (A and B) Effects of varying the wavevector $\tilde{q}$ around $0.333\ Q_0$ by $\pm 1\%$ and $\pm 2\%$, respectively. (C and D) Effects of varying the gap value $\tilde{\Delta}$ around 12 meV by $\pm 10\%$ and $\pm 20\%$, respectively. Error bars for $\tilde{q}(0.004\ Q_0)$ and $\tilde{\Delta}$ (2 meV) are deduced using these variations.
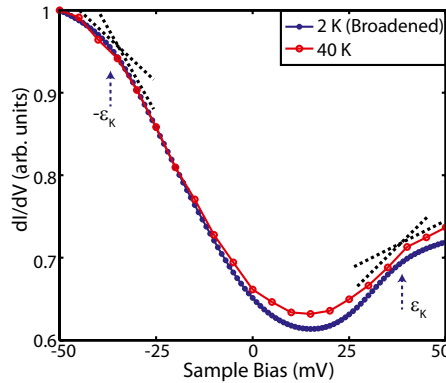
Fig. S6. Spectroscopy above T_{CDW}. Spectrum acquired at 40 K (red) compared with that acquired at 2 K, 6 T (blue) on the same cleaved surface (within 300 nm). The 2 K spectrum has been thermally broadened to 40 K for ease of comparison. The spectral kinks at ± 35 mV ($\pm \varepsilon_K$) are distinguishable well above T_{CDW}, as shown by the guides to the eye (see Fig. 1C for a low-temperature comparison).
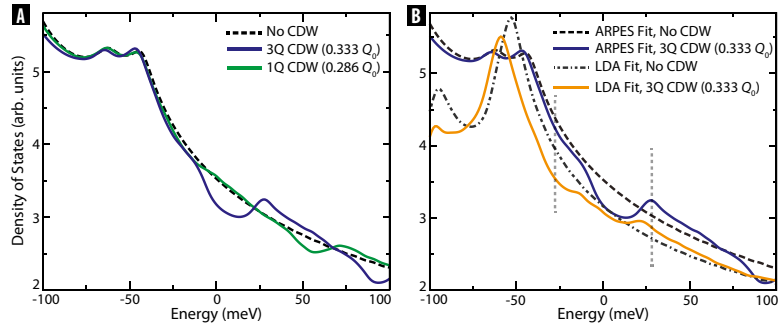
Fig. S7. Comparisons of DOS calculations. (A) Calculated DOS spectrum using the ARPES tight-binding fit in the presence of a 3Q CDW ($\tilde{q} = 0.333\ Q_0$; blue) and a 1Q CDW ($q_{1Q} = 0.286\ Q_0$; green), with $\tilde{\Delta} = 12$ meV. (B) Calculated DOS spectrum using the tight-binding fit to ARPES data (13) compared with a tight-binding fit to LDA calculations (11) in the "normal" state and in the presence of a 3Q CDW ($\tilde{q} = 0.333\ Q_0$, $\tilde{\Delta} = 12$ meV). The DOS spectrum calculated using the fit to the ARPES data better reproduces the gap feature observed in the STM dI/dV spectrum in Fig. 5C.

Table S1. Tight-binding parameters for the two Nb bands (in meV)

Parameter	Nb band 1	Nb band 2
t_0	26.9	219.0
t_1	86.8	46.0
t_2	139.9	257.5
t_3	29.6	4.4
t_4	3.5	−15.0
t_5	3.3	6.0